Construction and Building Materials 364 (2023) 129957

Contents lists available at ScienceDirect

Construction and Building Materials

journal homepage: www.elsevier.com/locate/conbuildmat

Reactivity of BOF slag under autoclaving conditions

J.C.O. Zepper [a,*], S.R. van der Laan [a,b], K. Schollbach [a], H.J.H. Brouwers [a]

[a] *Department of the Built Environment, Eindhoven University of Technology, Eindhoven 5600 MB, The Netherlands*
[b] *Tata Steel, R&D, Microstructure & Surface Characterization (MSC), P.O. Box 10.000, 1970 CA IJmuiden, The Netherlands*

ARTICLE INFO

Keywords:
BOF slag
Reactivity
Hydrothermal activation
Microstructure
Mineralogy
Hydrogarnet

ABSTRACT

Basic oxygen furnace (BOF) slag is an industrial by-product of the steel industry and is currently used only in low-end applications like road fill or is landfilled. This study explores the possibility of BOF slag as raw material in the building industry by investigating its reactivity under autoclave conditions. The results reveal that autoclaving improves the mechanical performance as well as increases the reactivity based on the degree of hydration in BOF slag containing samples. Although, >40 wt% of hydration product (α-C_2SH, hydrogarnet, portlandite and amorphous) was formed after autoclaving, autoclaved BOF slag containing samples show poor mechanical performance.

1. Introduction

Basic oxygen furnace slag (BOF slag), which is also known as Linz-Donawitz slag (LD-slag) is the industrial by-product of steel making. BOF slag is produced together with steel during the converter process [1]. In the converter process carbon-rich hot metal, which is derived from the blast furnace, is converted to low-carbon steel. There are two reasons why the resulting BOF slag from this process could be used as a cement replacement. One reason is comparable phase composition with major phases that are present in cement also being present in sufficient amounts in BOF slag such as $C_2(A,F)$ and C_2S. The second reason is the large availability of BOF slag, which is approximately 10 wt% of the produced amount of steel from the converter process.

However, there are certain properties of the BOF slag that limits its use as supplementary cementitious material (SCM). The presence of free lime and free MgO can cause large volume expansion when hydrating [2,3] and it has also low hydraulic reactivity as shown by previous isothermal calorimetry experiments [4–6]. The low reactivity of BOF slag is mainly due to the absence of C_3S [7,8], but also the presence of oxides like MnO, P_2O_5 and V_2O_5 in significant amounts (>1 wt%) compared to cement may lower the reactivity of BOF slag [9,10]. In addition, previous research has shown that under normal curing conditions BOFS slag is not suitable as SCM with high replacement levels as BOF slag lowers the pH within the pore solution and inhibits the precipitation of portlandite resulting in the delay of C_3S hydration [11]. In general, replacement levels of BOF slag as an SCM are advised are about 20 wt% [12,13].

Autoclaving can address especially issue of low reactivity as it is a method for fast curing in a water steam environment in order to increase phase reactivity and product strength [14,15]. Hence, autoclaving might solve the issues of low reactivity and delaying the hydration of C_3S. Usually, an autoclave treatment is applied to cure a highly cellular structure such as autoclaved aerated concrete (AAC) or produce dense sand-lime bricks. However, an autoclave treatment can also be applied to produce dense bricks from copper mine tailing, fly ash or reactive powder concrete [15–17]. Since BOF slag is a high density material [18] it lends itself to the production of dense autoclaved bricks rather than light-weight AAC. Therefore, our study concerns the application of BOF slag in an autoclaved cured brick.

Previous studies mainly focused on autoclaving BOF slag to improve volume stability by reacting the free lime and free MgO [19–21] or to produce AAC [4,22]. Few studies focused on the reactivity of the major phases (C_2S, $C_2(A,F)$ and wuestite) that are present in BOF slag. For example, Qian et al. [21] concluded that the reactivity of wuestite depends on the FeO/MgO ratio. The lower this ratio is, the higher the reactivity of the wuestite phases. The reaction product was mainly brucite ($Mg(OH)_2$). For C_2S it is been reported to form α-C_2SH between 120 and 180 °C under steam saturated autoclave conditions [23], whereas C_3A and C_2F can be used to synthesize hydrogarnets under hydrothermal conditions [24], which can be stable at least up to 250 °C [25]. However, there is little information has been to the overall reactivity of BOF slag under autoclaving conditions [20] even though it is an important requirement for the production of an actual building material. To further understand how the three primary BOF slag phases (C_2S,

---

* Corresponding author.
E-mail address: j.c.o.zepper@tue.nl (J.C.O. Zepper).

https://doi.org/10.1016/j.conbuildmat.2022.129957
Received 20 June 2022; Received in revised form 22 November 2022; Accepted 1 December 2022

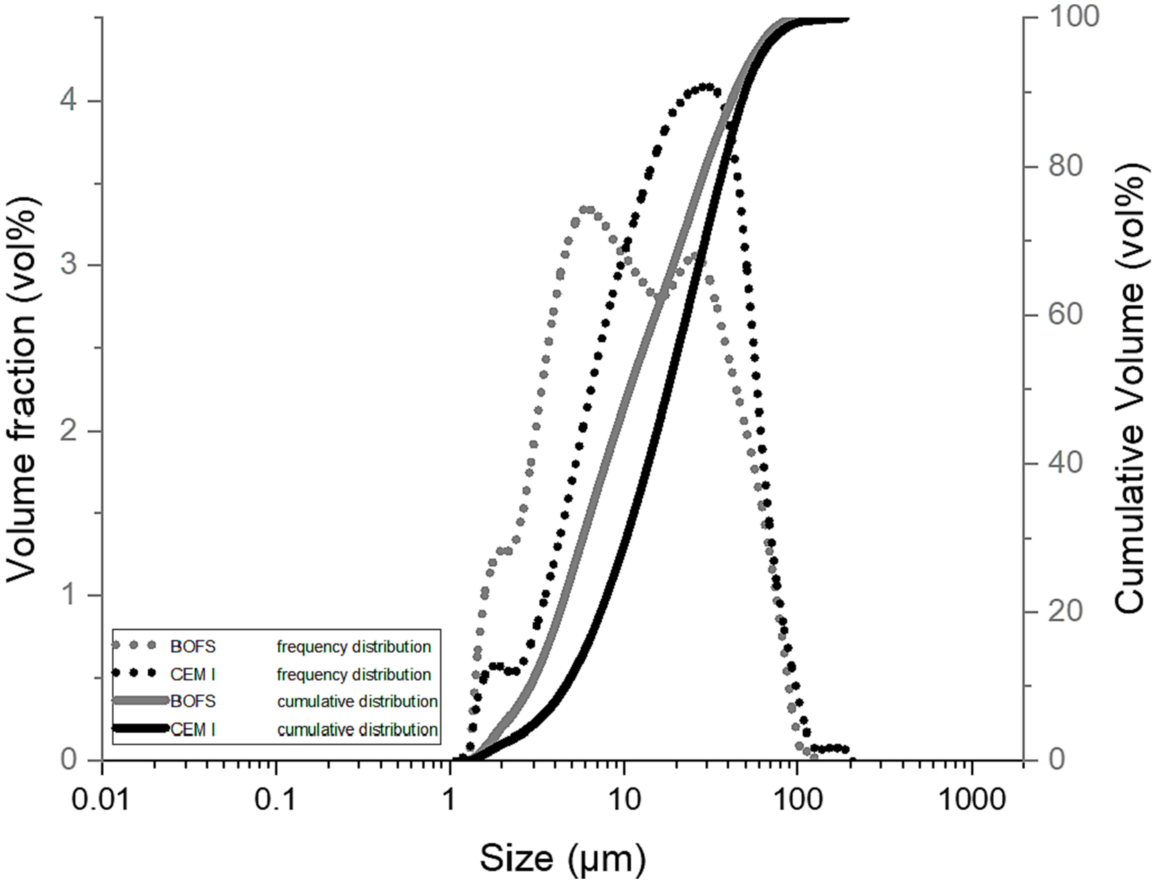

Fig. 1. Presents frequency (dotted lines) and cumulative (solid lines) particle size distribution of the milled BOF slag (black lines) and CEM I 42.5 N. (grey lines).

Table 1
XRF analysis and loss on ignition (LOI) of BOF slag and CEM I 42.5 N. For the BOF slag a negative LOI is reported due to weight gain caused by the oxidation of Fe^{2+} to Fe^{3+}. All Fe is reported as Fe_2O_3*, but it should be noted that Fe can occur in BOF slag as Fe^0, Fe^{2+} and Fe^{3+}. b.d.l. means below the detection limit.

	MgO	Al_2O_3	SiO_2	P_2O_5	SO_3	CaO	TiO_2	V_2O_5	Cr_2O_3	MnO	Fe_2O_3*	ZnO	Total	LOI
BOF slag	7.78	2.04	14.1	1.63	b.d.l.	40.3	1.38	1.04	0.30	4.71	26.7	b.d.l.	100	−0.6
CEM	1.75	4.71	18.4	0.31	2.81	67.8	0.43	b.d.l.	b.d.l.	0.11	3.64	0.11	100	1.7

Table 2
Presents the results of the spread flow test and the addition of superslasticizer at w/b of 0.25.

Sample	Spread diameter (cm)	Superplasticizer (wt%)
BOFS 100	23	–
BOFS 50	20	0.1
CEM 100	20.5	0.2

$C_2(A,F)$ and wuestite) react together under hydrothermal conditions and learn more about the applicability of BOF slag as a raw material for the building industry we conducted a comprehensive study of BOF slag under autoclave conditions. This research consist of a multi-analytical approach to assess the hydration and the influence on strength quantitatively. In order to achieve this goal three samples with different initial compositions were prepared: pure BOF slag paste, pure cement paste and a 50:50 mix by mass at similar w/b ratios (0.25) in order to be comparable in terms of reactivity and microstructure. All samples were cured at room temperature for 72 h to produce green bodies, before autoclaving. Both green bodies and autoclaved samples were investigated using Rietveld quantitative phase analysis (QXRD), thermogravimetric analysis (TGA), Large-Area phase mapping (PARC) based on SEM/EDX, He-pycnometry and mercury intrusion porosimetry (MIP). Moreover, mechanical performance and leaching properties were tested, as well.

2. Materials and methodology

2.1. Materials and mixing design

Two types of raw materials, BOF slag and CEM I were used in the study, which are referenced with “I” at the end when they are mention in figures and tables. The BOF slag used in this study is supplied by the Tata Steel plant in IJmuiden, The Netherlands, and is representative of the standard BOF slag production. It was crushed to a size of < 5.6 mm. In order to apply the BOF slag as a binder, it was ground with a Retsch RS 300 XL discmill until the particle size distribution was comparable to CEM I 42.5 N (supplied by Heidelberg Cement Group). The PSD of both materials is illustrated in Fig. 1 and the chemical composition is given in Table 1. The PSD was determined with laser diffraction using a Malvern Mastersizer 2000.

Three paste mixes were prepared all with a water/binder (w/b) ratio of 0.25, in order to be comparable in terms of water content and because the BOF slag has a very low water demand [26–28]. The similar water contents in the three paste mixes have the aim that it is possible to compare the developed microstructure and reactivity of the mixes

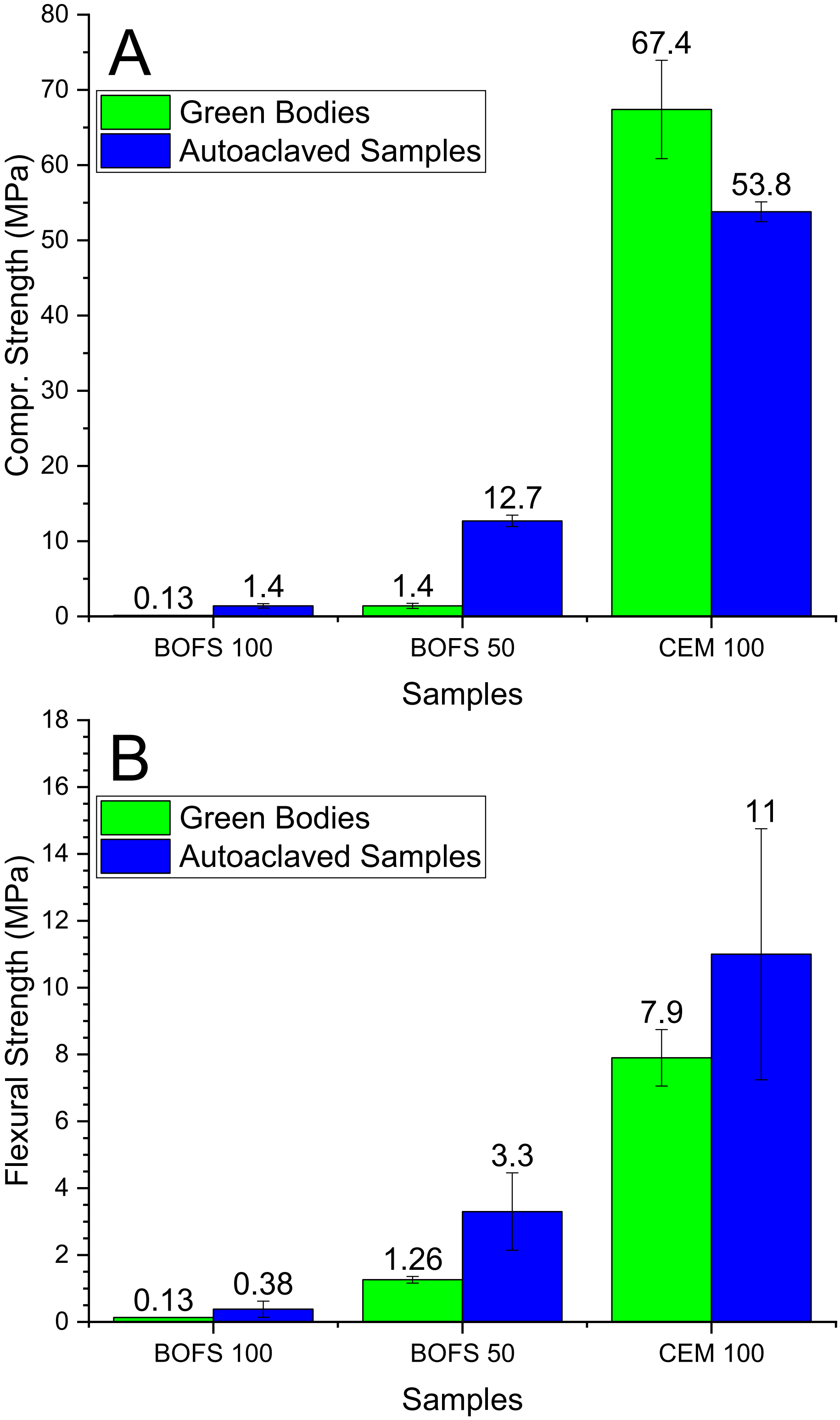

Fig. 2. Presents compressive (A) and flexural strength (B) results of normal cured for 72 h (green) and additional autoclave curing (blue). (For interpretation of the references to colour in this figure legend, the reader is referred to the web version of this article.)

because different w/b ratios would develop different microstructures (i.e. pore structure). The three pastes contained 100 wt% BOF slag (BOFS 100), 50 wt% BOF slag and 50 wt% CEM I (BOFS 50) and a reference sample with 100 wt% CEM I (CEM 100). Super plasticizer (Sika ViscoCrete – 264 con 35 % SPL) was added to achieve a comparable spread flow (Table 2). Subsequently, all pastes were mixed with a mixer for 5 min, casted in metal prism molds (4*4*16 cm) and covered with cling film.

2.2. Curing and autoclave treatment

For each mix six prisms were prepared. All six prism were first cured

Table 3
Reports the results of the rietveld quantitative phase analysis (QXRD) for initial raw materials (I), normal cured (72 h) samples (G) and autoclaved samples (A). Please note that BOFS 50 I * is calculated from 50 wt% BOF slag and 50 wt% CEM 1.

Phase Name	Cement Notation	BOFS 100 I	BOFS 100 G	BOFS 100 A	BOFS 50 I*	BOFS 50 G	BOFS 50 A	CEM 100 I	CEM 100 G	CEM 100 A
Wuestite	RO-Phase	24.3	20.9	14.8	12.1	10.6	7.0			
Belite	C_2S	42.4	36.6	22.6	30.4	24.0	14.6	18.4	11.6	12.8
Magnetite	Ff	6.4	6.0	6.7	3.2	3.5	3.5			
Brownmillerite	$C_2(A,F)$	18.4	13.5	8.5	14.3	9.5	6.8	10.3	8.8	8.1
Alite	C_3S	0.2	0.1	0.7	27.7	16.8	6.4	55.2	16.6	7.4
Free Lime	C	0.6	0.5	0.3	0.3	0.3	0.2			
Portlandite	CH	0.8	0.9	2.7	0.6	3.2	6.5	0.4	10.4	13.5
Calcite	Cc	0.3	0.3	2.0	0.9	0.7	1.9	1.6	1.9	1.6
Celite	C_3A				2.2	1.7		4.3	0.9	2.2
Hydrogarnet	$C_3(A,F)S_{3-x}H_{2x}$		2.4	7.3		1.2	10.6		1.3	7.6
Ettringite	$C_6AS_3H_{32}$					2.6			2.9	0.6
Jaffeite	$C_6S_2H_3$									5.2
Tobermorite	$C_5S_6H_5$						1.2			11.6
α-C_2SH	C_2SH			15.0			23.0			
Brucite	Mc			0.9			0.7			
Metavauxite	fAP_2H_9			1.4						
Others		1.9	2.4	0.2	2.7	5.5	1.2	3.6	4.4	1.7
Amorphous		4.7	16.4	17.0	5.5	20.2	16.4	6.3	41.2	27.6
Total		100	100	100	100	100	100	100	100	100
GOF		1.19	1.23	1.3	*	1.46	1.56	1.83	1.64	2.01
Rwp		1.71	1.78	3.55	*	2.54	5.37	4.35	3.66	9.82

72 h at room temperature before demolding. Half of the prisms were then autoclaved. The autoclaved samples are referenced with “A”, whereas the samples that were only cured at room temperature for 72 h are labeled “G” for green bodies. The initial materials are labeled with “I”. The long curing time was applied because BOF slag reacts very slowly and did only achieve sufficient strength for demolding before 72 h. The hydration was stopped after strength testing by double solvent exchange method with isopropanol and diethyl ether according to [29] after 72 h and autoclaving to perform further analysis on the samples.

The autoclave treatment was performed at HESS AAC Systems in Enschede, The Netherlands, in a Scholz saturated steam laboratory autoclave with a diameter of 50 cm and cylindrical length of 70 cm. The steam was generated by a WIMA-Steam Generator Type ED. The autoclave treatment was for 8 h with linear increasing pressure for 1.5 h to a maximum pressure and temperature of 11 bar and 187 °C. The holding time at the maximum autoclave conditions was 5 h. Subsequently, pressure was decreased linear for the final 1.5 h (Fig. A1 Appendix).

2.3. Methodology

Flexural strength of the green bodies and autoclaved samples was determined on prisms (4 * 4 * 16 cm^3) and compressive strength on the halves according to EN 196-1.

Thermogravimetric analysis (TGA) was performed on a Jupiter STA 449 F1 Netzsch by using 40 – 60 mg powdered sample. The measurement was performed under a nitrogen atmosphere with a heating rate of 10 °C/min with a maximum of 1000 °C.

Mercury intrusion porosimetry (MIP) was performed on 2 – 4 mm fragments (0.6 – 0.9 g of sample) of the autoclaved samples. The measurement instrument was AutoPore IV 9500 Micromeritics Series Mercury Porosimeter, and a maximum pressure of 228 MPa, assuming a contact angle of 130° for the evaluation.

X-ray fluorescence analysis was performed on the initial materials (BOF slag and CEM I 42.N). Prior to the analysis the raw materials were heated up to 1000 °C in order to determine the loss (CEM I) or gain (BOF slag) on ignition. After loss on ignition, fused beads were produced by using the flux lithium borate ($Li_2B_4O_7$:$LiBO_2$ = 65:35). The weight proportions that were used between sample to borate was 1:10. The analysis was performed on a PANalytical Axios.

XRD analysis was performed on powdered material (initial materials and green bodies, autoclaved samples after stopping hydration). Prior to analysis 10 wt% Si-metal was added as an internal standard and 7 ml cyclohexane was added as grinding aid. Grinding was performed with a Retsch McCrone micronizer mill for 20 min. After sample recovery, cyclohexane was evaporated in drying oven for 5 min at 70 °C and the powder was subsequently back-loaded on a metal sample holder. The XRD measurement of the initial raw materials and green bodies was performed on a Malvern PANAlytical XpertPro with a Co anode and Pixel 3D detector. A fixed divergence slit of 0.5° and 0.04 rad soller were used. The autoclaved materials were analyzed with Bruker D8 X-ray diffractometer equipped with a Co anode and a LynxEye detector, a fixed divergence slit of 0.5° and primary and secondary collimeter of 2.5°. The 2θ range used for measurements with both instruments was 10 – 120°. In the first step of analysis of the XRD powder pattern, phases were identified with HighScore Plus 3.0.5. QXRD was performed with Topas 5. The structures of the identified phases that were used for the Rietveld quantitative phase analysis (QXRD) were taken from the AMCS, ICDS or PDF database (Appendix Table A1).

Prior to measuring scanning electron microscopy (SEM) combined with energy-dispersive X-ray spectroscopy (EDX) on the autoclaved materials, they were cut into 5–7 mm thick slices and immersed for 72 h in isopropanol and then vacuum dried at 40 °C for 24 h. The slices were embedded in epoxy resin (Struers EpoFix), polished and subsequently coated with carbon. Data collection for spectral imaging for large-area phase mapping was performed with a JEOL JSM-7001F SEM, two 30 mm^2 SDD detectors (Thermo Fischer Scientific) and NORAN-System7 hardware with NSS.3.3 software. The accelerating voltage was 15 kV with a beam current of 6.2nA. In total, 36 connected spectral imaging fields were collected for each autoclaved material sample with each field consisting of 512x384 pixels (pixel size 1 μm^2). The collected spectral imaging fields were stitched together and analyzed with PhAse Recognition and Characterization software (PARC) and sum spectra were derived for the chemical composition of the PARC phases. The sum spectrum contains the cumulative of EDX spectra of all “clean” pixels for one defined PARC phase. For a more detailed description on PARC, the reader is referred to [30]. The resulting data was used to determine the chemical composition of initial phases and hydration products. Moreover, PARC is used for an area-proportional quantification of the phase amounts in area%.

One batch leaching tests were performed on the autoclaved samples according to EN12457-2. 20–30 g of autoclaved material was put in the polyurethane bottles. Ultra-pure water was added within a liquid/solid

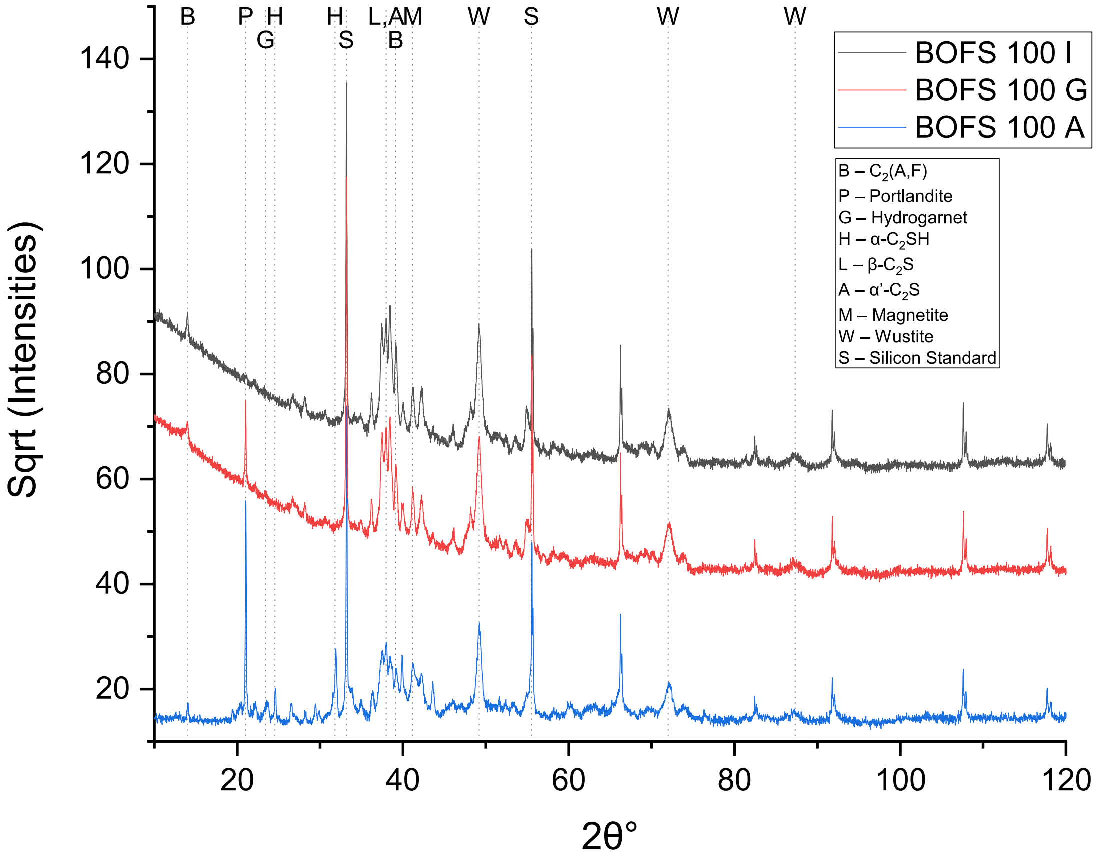

Fig. 3. Illustrates XRD patterns of BOFS 100 I (black), BOFS 100 G (red) and BOFS 100 A (blue) and the identified phases (legend on the right). (For interpretation of the references to colour in this figure legend, the reader is referred to the web version of this article.)

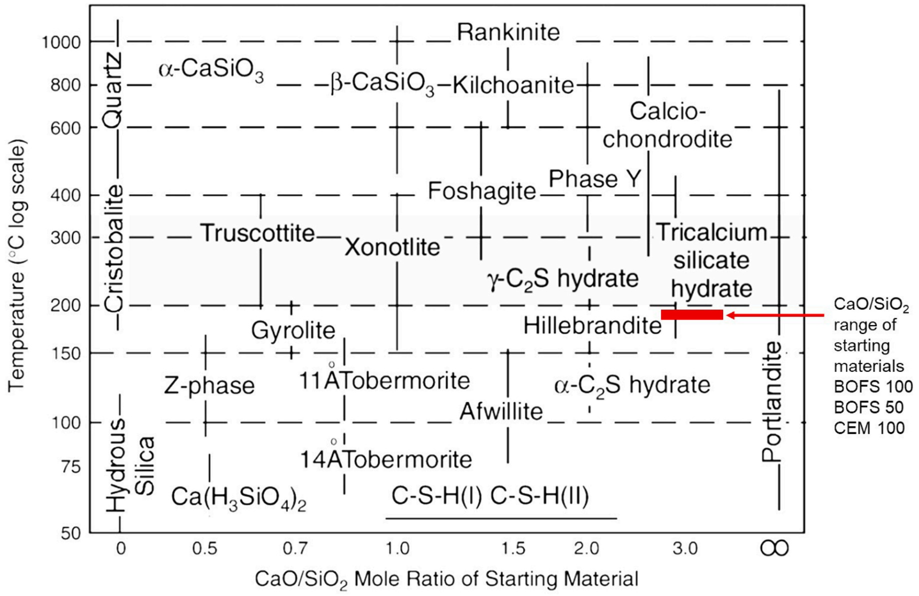

Fig. 4. Presents $CaO\text{-}SiO_2\text{-}H_2O$ phases from 50 to 1000 °C, modified after Meller [18]. CaO/SiO_2 molar ratios are indicated by vertical lines. It should be noted that as emphasized by Taylor [25] that the diagram presents not equilibrium conditions but “merely represents the conditions under which each phase is most usually obtained”. Red bar presents the range of CaO/SiO_2 molar ratio of the starting mixes in this study. BOFS 100 and CEM 100 are located at the left and right end of the bar and, respectively. (For interpretation of the references to colour in this figure legend, the reader is referred to the web version of this article.)

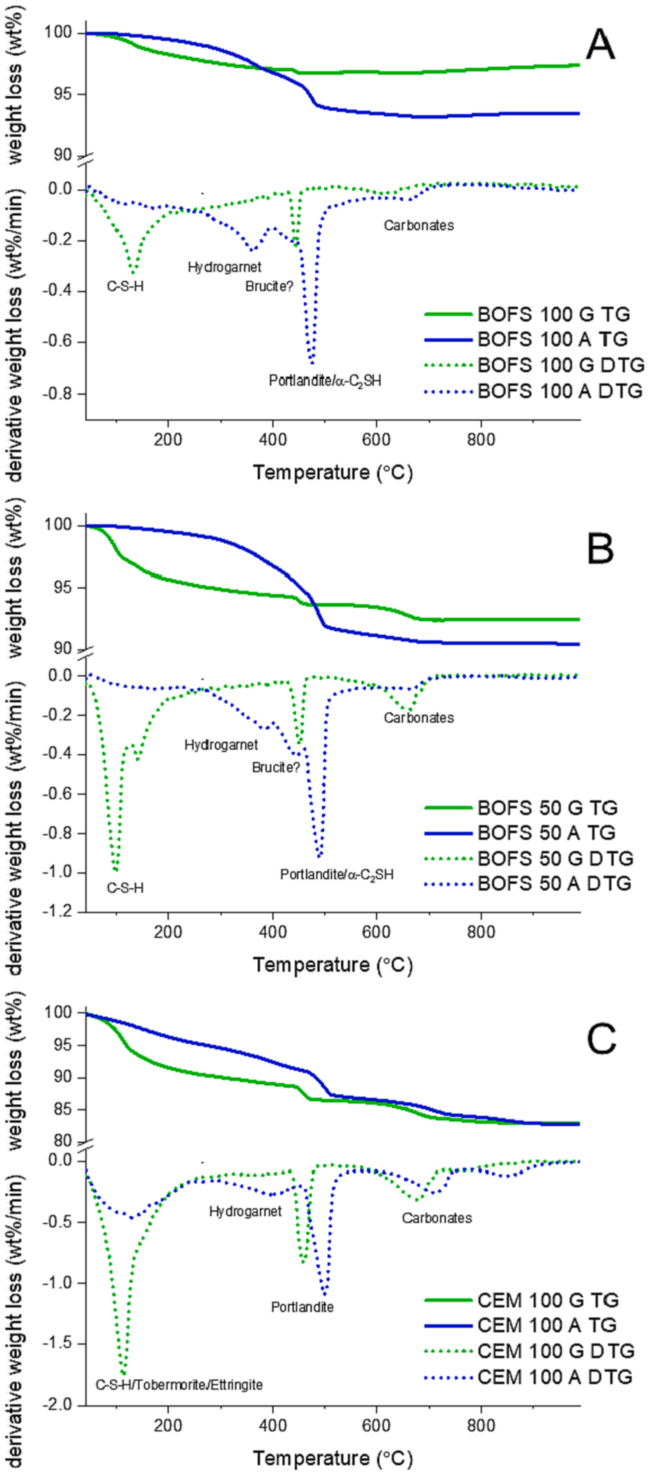

Fig. 5. Presents the TGA (solid lines) and DTGA (dotted lines) of normal cured (green) and additionally autoclaved cured (blue) samples, with BOFS 100 (A), BOFS 50 (B) and CEM 100 (C). (For interpretation of the references to colour in this figure legend, the reader is referred to the web version of this article.)

ratio of 10 to act as the leachant. The filled bottles were shaken with a dynamic shaker for 24 h at a constant speed of 250 rpm. Subsequently, the leachate was centrifuged for 10 min at 3500 rpm decanted and filtered with a syringe filter with a pore diameter of 0.22 µm. The pH was the determined by using a calibrated Volcraft PH-100 ATC pH-meter. The leachates were then acidified with concentrated HNO_3. The measurement was performed on a Spectroblue inductive coupled plasma atomic emission spectrometer (ICP-OES), according to NEN 6966.

3. Results and discussion

3.1. Mechanical strength of autoclaved BOF slag as building material

The mechanical strength of green bodies and autoclaved samples is compared in order to evaluate the autoclave treatment. The compressive and flexural strength of the green bodies after curing for 72 h is increasing with increasing amount of CEM I 42.5 N (Fig. 2). BOF slag green bodies have very low compressive and flexural strengths (<2 MPa). After 8 h of autoclaving BOF slag containing samples show a tenfold increase in compressive strength, but the overall strength remains very low. BOFS 100 and BOFS 50 increase from 0.1 to 1.4 MPa and 1.4 to 12.7 MPa, respectively. The CEM 100 sample decreases in strength from 67.4 to 53.8 MPa after autoclaving. The compressive strength value of the CEM 100 A is comparable to earlier reported compressive strength values of 63 MPa for autoclaved cement pastes [18]. Like the compressive strength, the flexural strength for BOF slag containing samples increase from 0.13 to 0.4 MPa (BOFS 100) and from 1.26 to 3.3 MPa (BOFS 50) after autoclaving.

3.2. Phase composition before and after autoclaving

Table 3 gives the results of the QXRD for the raw materials (milled BOF slag and CEM I 42.5 N), green bodies and autoclaved samples. XRD pattern of all samples are presented in Fig. 3 (BOFS 100) and Fig. A2 Appendix (BOFS 50 and CEM 100). The initial phase composition of the BOF slag consisted of 4 major phases. C_2S (42.3 wt%), wuestite (24.3 wt %), $C_2(A,F)$ (18.4 wt%) and Magnetite (6.4 wt%). Only low amounts of free lime were found (0.6 wt%). After 72 h of curing at room temperature minor amounts of hydrogarnet (2.4 wt%) were detected and the amorphous content increased to 16.4 wt% in the BOFS 100 G sample. After the subsequent autoclave treatment hydrogarnet content increased to 7.3 wt%, while the amorphous content barely changed (17 wt%) and one new phase had formed (α-C_2SH; 15 wt%). α-C_2SH develops under hydrothermal conditions (above 100 – 150 °C, at pressures > 1 bar) for Ca/Si molar ratio of > 1.5 [25,32]. Even though the autoclave treatment (187 °C and 11 bar) was outside of the stability field of α-C_2SH [33], allegedly this phase forms due to the long reaction time to form hillebrandite from α-C_2SH or the presence of foreign ions such as Fe^{3+} and Al^{3+} which may stabilize α-C_2SH at different temperatures [25,33–35]. This is also illustrated by Fig. 4, which presents the most common phases occurring under hydrothermal conditions in the CaO-SiO_2-H_2O system [32]. However, it has been previously reported that α-C_2SH may occur in autoclaved OPC paste samples [36,37].

The initial phase composition of the CEM 100 I consisted of 4 major phases, C_3S (55.2 wt%), C_2S (18.4 wt%), $C_2(A,F)$ (10.3 wt%) and C_3A (4.3 wt%). After 72 h of curing at room temperature portlandite content was 10.4 wt% and amorphous content was 39.2 wt%. The subsequent autoclave treatment reduced the amorphous content to 27.6 wt% and increased portlandite and hydrogarnet content to 13.5 and 7.6 wt%, respectively. Moreover after autoclaving CEM 100 A contained 28.3 wt % of residual cement phases (C_3S, 7.4 wt%; C_2S, 12.8 wt% and $C_2(A,F)$, 8.1 wt%).

The initial composition of BOFS 50 was calculated by using the results of the QXRD of the pure raw materials. This calculated phase composition consisted of wuestite (12.1 wt%), C_2S (30.4 wt%), $C_2(A,F)$ (14.3 wt%) and C_3S (27.7 wt%). After 72 h of curing at room temperature BOFS 50 G contained 3.2 and 19.5 wt% portlandite and amorphous content, respectively as the main reaction products. After autoclaving BOFS 50 A contained 6.5, 10.6 and 16.4 wt% portladite, hydrogarnet and amorphous content. Moreover, BOFS 50 A 23 wt% of α-C_2SH. A complete overview of the QXRD can be found in Table 3.

When comparing the series of green bodies (BOFS 100 G, BOFS 50 G and CEM 100 G), the most obvious difference is the increase in

Table 4
Presents weight losses by TGA per selected temperature intervals.

Sample	Weight loss in temperature interval (wt%) 80–200 °C	200–400 °C	400–600 °C	40–1000 °C
BOFS 100 G	1.54	1.19	0.28	2.61
BOFS 100 A	0.49	2.72	3.31	6.50
BOFS 50 G	3.63	1.27	0.96	7.50
BOFS 50 A	0.46	2.80	5.58	9.55
CEM 100 G	7.07	2.56	2.96	17.08
CEM 100 A	3.17	3.93	5.89	17.24

amorphous and portlandite content with increasing amount of CEM I, which increases from 16 (BOFS 100 G) to 39 wt% (CEM 100 G) and 0.9 to 10.4 wt%, respectively due to the hydration of C_3S. Moreover, we see differences in the reaction products that have developed during the hydration in the first 72 h. Whereas CEM 100 G is mostly dominated by the formation of amorphous phase and portlandite, BOFS 100 G shows also minor amounts of hydrogarnet (2.4 wt%). The formation of hydrogarnet during the hydration of BOF slag has been reported before [26,27]. The difference in hydration products between BOF slag and CEM I further increases when comparing the phase composition of the autoclaved samples. BOFS 100 A is dominated by the formation of hydrogarnet, α-C_2SH, portlandite and amorphous phase, CEM 100 A is dominated by tobermorite, portlandite, jaffeite and amorphous content. BOFS 50 A has significantly higher α-C_2SH (23 wt%) compared to BOFS 100 A (13.2 wt%) and no α-C_2SH was detected in the CEM 100 A sample.

These results do not correspond to the expected phases according to phase diagrams of the $CaO\text{-}SiO_2\text{-}H_2O$ system [25,33] under hydrothermal conditions (>100 °C). Commonly phase diagrams show for calcium silicate hydrates at hydrothermal conditions that the phase assemblages depend on temperature and Ca/Si ratio of the initial materials (Fig. 4). The phase diagrams are not applicable to our results because the system has not reached equilibrium as can be inferred from the large amounts of initial unreacted phases that still persist, as identified by QXRD. Moreover, the system at hand is not a pure $CaO\text{-}SiO_2\text{-}H_2O$ system plays, which would play a significant role as well [31,32,35,38,39]. At the end, the large amount of reaction products (i.e. hydrogarnet, α-C_2SH and amorphous) observed in BOFS 100 A and BOFS 50 A does not translate to high strength. As explained in Taylor [35], this might be related to the formation of α-C_2SH at the expanse of C—S—H phases. α-C_2SH forms crystals with a rectangular tablet-like habitus causing porosity and a low strength material. How much porosity forms is further discussed with evaluation of the MIP results.

BOF slag reactivity under autoclave conditions can also be determined by using TGA in order to compare the bound water between samples cured at room temperature and autoclaved material (Fig. 5, Table 4). The CEM 100 G sample shows the highest amount of mass loss during TGA of all green bodies with 17.1 wt%, whereas the BOFS 100 G has the lowest amount of weight loss (2.6 wt%) illustrating the low early reactivity of BOF slag [5]. However, after autoclaving the BOFS 100 sample, the total mass loss increased to 6.5 wt% (BOFS 100 A) indicating improved reactivity under autoclave conditions. All green body samples (BOFS 100 G, BOFS 50 G and CEM 100 G) show three major peaks in the DTG – curves. The first one between 80 and 175 °C can be assigned to C—S—H and ettringite, the second one between 450 and 550 °C to portlandite and the third one at around 700 °C to the decomposition of carbonates [29,40]. Although QXRD shows the presence of hydrogarnet a clear hydrogarnet DTG peak (200 – 400 °C) is absent in the green body samples, because the content is low and probably overlaps with other weigh loss reactions.

After autoclaving the C—S—H peaks largely disappear in all three samples, because it reacts to α-C_2SH or jaffeite [37], whereas the α-C_2SH

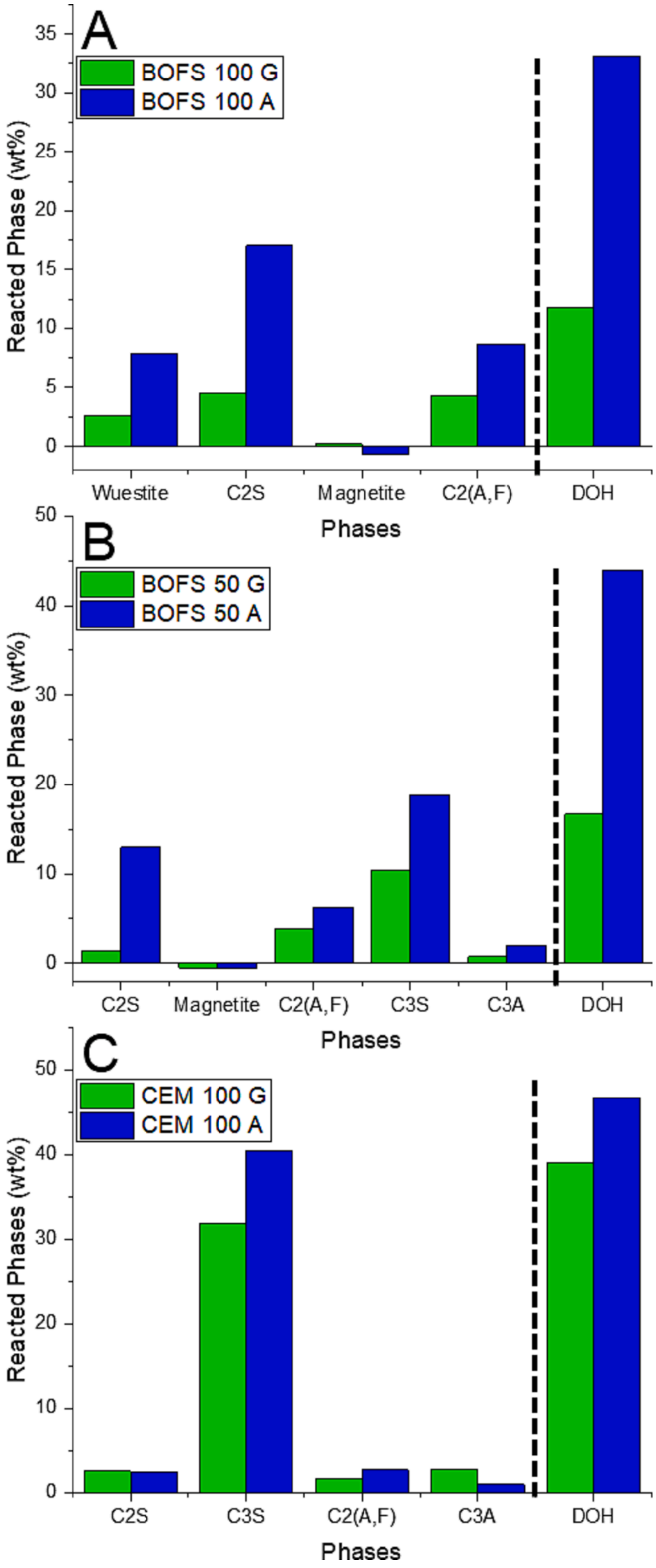

Fig. 6. Illustrates the degree of hydration (DOH) and the normalized phases amounts of initial major phases (>2 wt%) that have reacted for normal and autoclaved cured samples. The DOH is a measure to assess how much the initial phases have reacted. The DOH is calculated by using the sum of the normalized initial phases that have contributed to the reaction products.

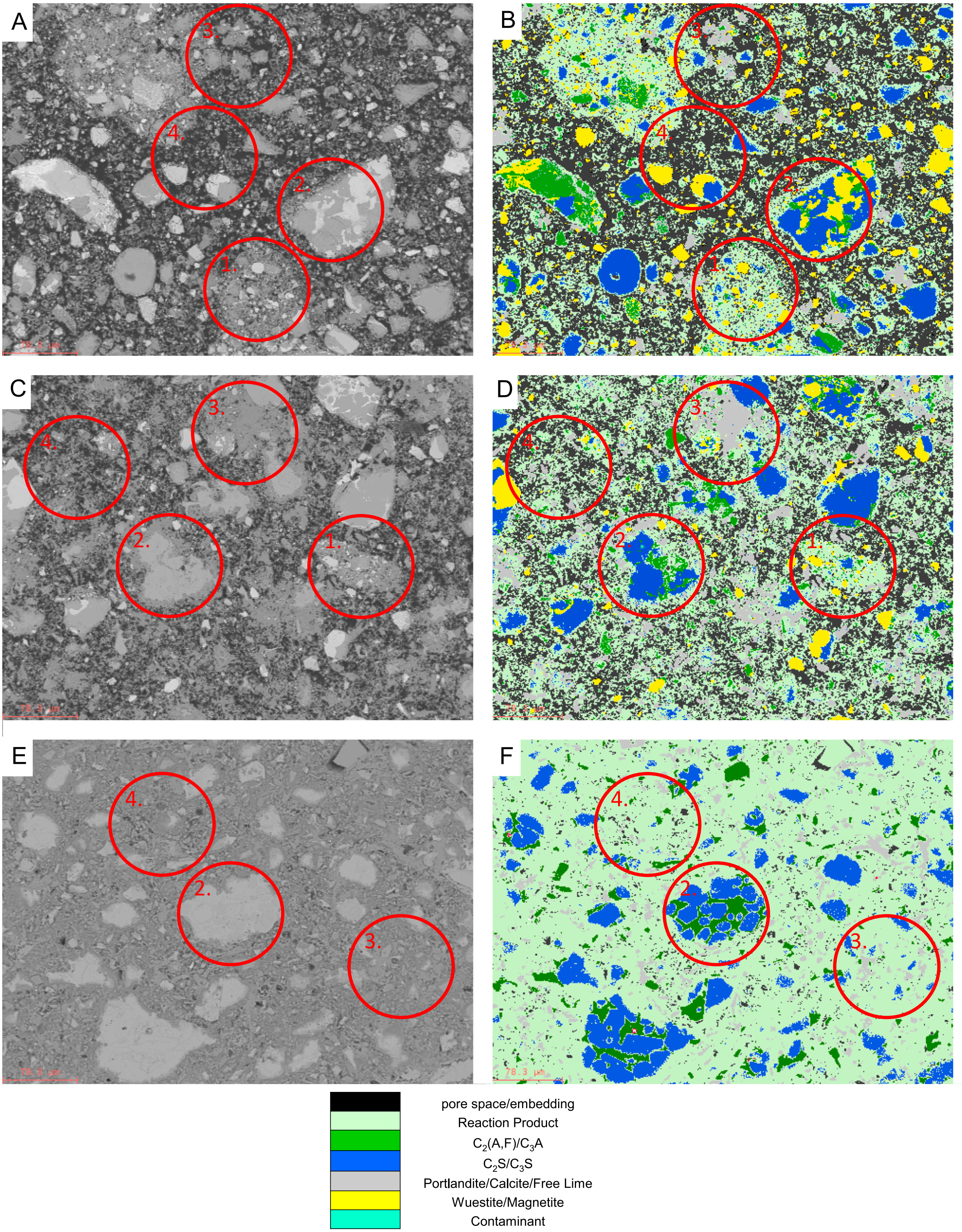

Fig. 7. Presents SEM (A, C and E) and the respective PARC phase maps (B, D and F) of the autoclaved samples BOFS 100 A (A and B), BOFS 50 A (C and D) and CEM 100 A (E and F). All figures represent one field (512 × 384 µm) of the total phase mapping of 36 fields. Additionally, the four main microstructure types are circled red (see text for more information), whereas microstructure type 1 is absent in CEM 100 A. (For interpretation of the references to colour in this figure legend, the reader is referred to the web version of this article.)

Table 5
Presents the results of the PARC analysis with the PARC phase Area% and their respective chemical composition in oxide wt%.

BOFS 100 A	Area%	Na_2O	MgO	Al_2O_3	SiO_2	P_2O_5	SO_3	K_2O	CaO	TiO_2	V_2O_5	Cr_2O_3	MnO	Fe_2O_3*	Total
Reaction Product	51.0	0.0	2.4	1.8	22.7	3.0	0.3	0.0	48.3	2.1	1.4	0.7	2.0	15.4	100.0
C_2S/C_3S	17.7	0.1	0.1	0.3	29.5	3.2	0.2	0.0	62.0	1.2	0.8	1.3	0.0	1.3	100.0
$C_2(A,F)$	5.8	0.0	0.7	8.6	2.4	0.1	0.1	0.0	42.2	9.2	1.9	0.4	1.4	33.0	100.0
Wuestite/Magnetite	15.6	0.0	23.6	0.0	0.6	0.0	0.0	0.0	2.5	0.0	0.1	0.5	13.2	59.4	100.0
Portlandite/Calcite/Free Lime	9.9	0.0	0.7	0.4	2.0	0.4	0.2	0.0	90.8	0.8	0.1	0.1	0.9	3.7	100.0
Bulk PARC		0.0	7.0	1.5	15.3	1.9	0.2	0.0	42.2	1.8	0.9	0.7	4.3	24.2	100.0
BOFS 50 A															
Reaction Product	62.5	0.3	2.6	3.1	24.6	1.8	2.7	0.1	54.6	1.2	0.4	0.7	0.9	7.1	100.0
C_2S/C_3S	12.9	0.2	0.4	0.6	28.1	2.4	0.3	0.0	64.1	1.1	0.6	1.2	0.0	1.2	100.0
$C_2(A,F)/C_3A$	5.7	0.1	1.4	12.0	2.8	0.2	0.1	0.1	43.2	6.9	1.4	0.1	1.2	30.6	100.0
Wuestite/Magnetite	5.7	0.0	22.6	0.1	0.5	0.0	0.0	0.0	2.8	0.0	0.1	0.5	13.6	59.7	100.0
Portlandite/Calcite/Free Lime	13.1	0.2	0.6	0.7	2.6	0.4	0.7	0.1	91.9	0.7	0.1	0.1	0.4	1.9	100.0
BULK PARC		0.2	4.1	3.7	16.3	1.3	1.6	0.1	52.3	1.9	0.5	0.6	2.2	15.4	100.0
CEM 100 A															
Reaction Product	63.6	0.3	1.7	3.3	29.1	0.6	4.5	0.2	57.6	0.6	0.0	0.7	0.0	1.5	100.0
C_2S/C_3S	12.2	0.3	1.2	1.1	25.2	0.7	0.5	0.2	68.3	0.6	0.0	1.1	0.0	0.9	100.0
$C_2(A,F)/C_3A$	9.0	0.4	4.4	22.0	5.6	0.3	1.0	0.2	49.1	1.3	0.0	0.0	0.3	15.3	100.0
Portlandite/Calcite/Free Lime	15.1	0.1	0.5	0.7	4.9	0.3	1.0	0.1	91.3	0.6	0.0	0.2	0.0	0.4	100.0
BULK PARC		0.3	1.7	4.9	21.8	0.5	2.8	0.2	63.4	0.7	0.0	0.6	0.0	3.0	100.0

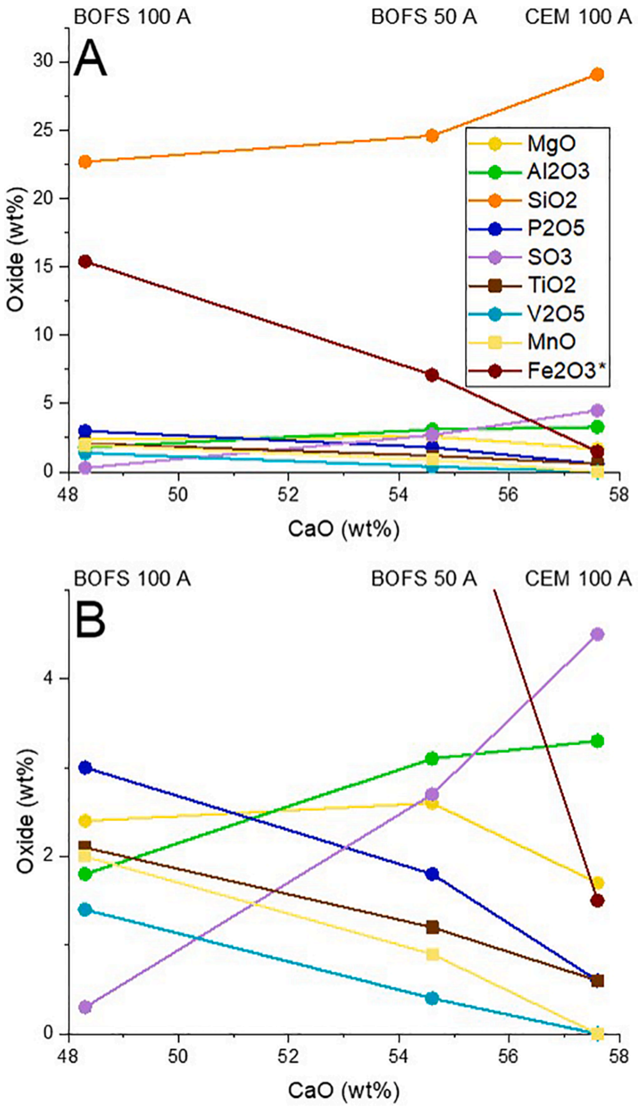

Fig. 8. A and B presents a variation diagrams to identify by which oxides BOFS 50 A is characterized.

peak is often overlaid by the portlandite peak between 400 and 500 °C [41]. Additionally, broad peak of hydrogarnet decomposition at around 375 °C appears in the autoclaved samples matching the QXRD results. A small hump in the DTG-curve is observed in BOFS 50 A and BOFS 100 A between the hydrogarnet and portlandite/ α-C_2SH peaks, which is probably caused by the dehydration of brucite that formed during autoclaving, although only small amounts of brucite (<1 wt%) were detected by QXRD.

Furthermore, tobermorite contributes to the C—S—H peak in the CEM 100 A sample in the temperature range of 80 – 175 °C [42]. The most striking difference between normal cured and autoclaved samples is the difference between the onset temperature of weight loss for certain phases. For example in the CEM 100 G samples the dehydration of portlandite starts at 420 °C, whereas in CEM 100 A the dehydration starts at 460 °C. Different dehydration temperatures of portlandite have been observed in the past when freshly hydrated cement pastes were compared with 5 year old cement pastes [43,44].

By combining QXRD and TGA it is possible to derive how much of each initial phase has reacted during the curing at room temperature and the autoclave treatment [29]. This also makes it possible to calculate the total degree of hydration (DOH), by comparing the amount of initial phases with the amount of remaining initial phases after reaction. The solid mass of the samples increases during reaction because free water is consumed and incorporated in the reaction products. Hence, a normalization to a common basis is necessary in order to be able to compare QXRD results and assess how much of the initial phases have reacted. For a more detailed description of the method and the used equations the reader is referred to [29]. For the DOH calculation minor initial phases (<2 wt%) and initial amorphous content is excluded and the amount of bound water contained in each sample is based on the TGA mass loss up to 600 °C. Fig. 6 presents the results for the calculation of the DOH and how much each phase has reacted in the green bodies cured at room temperature and after autoclaving. In both cases, the DOH rises with the CEM I content. In turn this can be attributed to the increasing amount of C_3S with CEM I content, being the most reactive phase in a cementitious system. The reactivity of C_3S becomes apparent in the CEM 100 samples, where after 72 h of curing at room temperature 29.3 wt% of the initial C_3S have reacted and after autoclaving 41.1 wt%.

The autoclaving of the BOF slag containing samples increases the DOH from 11.8 to 33.2 wt% for BOFS 100 and from 15.8 to 44 wt% for BOFS 50. In that sense autoclaving was very effective in increasing the reactivity of BOF slag. During curing at room temperature, $C_2(A,F)$ and C_2S are the most reactive phases in the BOFS 100 G sample and

Table 6
Presents the results for the calculation of PARC phase area% (Table 5) to wt% based on the presented densities. Densities for the reaction products are assumed and other the other densities were calculated by using the weighed mean form the QXRD results. Additionally, the QXRD results for phases were summarized to compare the QXRD results to PARC phase wt% results. N.p. refers to phases that were not present.

	BOFS 100 A			**BOFS 50 A**			**CEM 100 A**		
PARC Phase	PARC (wt%)	XRD (wt%)	Density (g/cm^3)	PARC (wt %)	XRD (wt %)	Density (g/cm^3)	PARC (wt %)	XRD (wt %)	Density (g/cm^3)
Reaction Product	40.3	41.6	2.4	54.3	51.9	2.3	55.7	52.6	2.1
C_2S/C_3S	19.1	23.3	3.3	7.7	7.5	3.3	16.7	20.2	3.3
C_4AF/C_3A	7.5	8.7	3.9	16.0	21.0	3.6	12.4	10.4	3.3
Wuestite/Magnetite	25.3	21.5	4.9	10.6	10.5	4.9	n.p.	n.p.	n.p.
Portlandite/Calcite	7.8	5.0	2.4	11.4	9.1	2.4	15.1	16.6	2.4

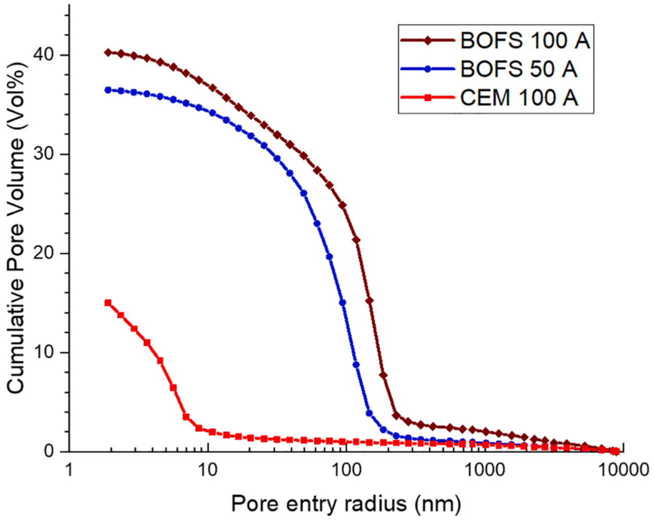

Fig. 9. Presents the results of MIP for autoclaved samples BOFS 100 A (brown line), BOFS 50 A (blue line) and CEM 100 A (red line). (For interpretation of the references to colour in this figure legend, the reader is referred to the web version of this article.)

Table 7
Presents the results of the ICP-OES analysis of the leachate for the autoclaved samples and the legal limits of the Dutch Soil Quality Degree (DSQD) for the most concerning elements. Additionally, the results of the pH measurement of the leachate is presented.

Elements	DSQD	BOFS 100 A	BOFS 50 A	CEM 100 A
As	0.9	b.d.l.	b.d.l.	b.d.l.
Cr	0.63	0.023	0.02	0.027
Pb	2.3	b.d.l.	b.d.l.	b.d.l.
V	1.8	b.d.l.	b.d.l.	b.d.l.
Zn	4.5	0.004	0.005	0.006
pH		12.5	12.5	12.4

contribute the most to the DOH (each 4 wt% each). The wuestite contributes slightly (2.7 wt%) in the formation of reaction products. This is surprising since it has been reported in the past to be an inert phase [27,45]. After autoclaving BOFS 100, C_2S is the most reactive phase, contributing 17.1 wt% to the DOH. But $C_2(A,F)$ and wuestite are also reacting contributing>8 wt% to the total DOH of BOFS 100 A, whereas magnetite does not contribute. The negative value of magnetite in Fig. 6 reflects minor amounts of formation by oxidation of wuestite during autoclave treatment. Another interesting feature that has been observed when evaluating the DOH data is that BOF slag delays the early hydration of CEM I. This feature is obvious when comparing the DOH values for C_3S in BOFS 50 G and CEM 100 G. In CEM 100 G the DOH of C_3S is almost at 30 wt% whereas in BOFS 50 G DOH values are 10 wt% for C_3S. This confirms earlier findings that BOF slag has significant influence on the precipitation of portlandite and the pH value of the pore solution in a BOF slag – CEM I system [11,46].

3.3. *Microstructural investigation and phase mapping (PARC) results of the autoclaved material*

Fig. 7 presents SEM BSE images and PARC phase maps based on EDX spectral imaging of the autoclaved samples. Four main microstructure types (Fig. 7, red circles) can be identified in the autoclaved samples: 1. primary finer BOF slag grains (<30 μm) in an agglomerated dense matrix of reaction products; 2. Larger multiphase unreacted multiphase BOF slag or cement grains (30 – 100 μm) with a rim of reaction product; 3. Larger portlandite/calcite (20 – 100 μm) grains; 4. Predominantly porous areas with small amounts of reaction product and primary BOF slag (only in BOFS 100 A and BOFS 50 A) down to fine pores in a matrix of reaction product (CEM 100 A). All four microstructural types are present in the autoclaved BOF slag containing samples, whereas microstructural Type 1. is absent in the CEM 100 A sample due to the absence of BOF slag in that sample. It should also be noted that the microstructure types between BOFS 100 A and BOFS 50 A are slightly different. For example in BOFS 100 A portlandite grains are generally smaller (type 3.) and the pore space is generally larger (type 4) than in BOFS 50 A.

Table 5 shows the area% of each phase detected with PARC and its chemical composition. The following phases were distinguished: reaction product, C_2S/C_3S, $C_2(A,F)/C_3A$, wuestite/magnetite, portlandite/calcite/free lime. For convenience C_2S/C_3S and in the cement containing samples $C_2(A,F)/C_3A$, are each combined into one phase. Furthermore, it is not possible to differentiate between the oxidation states of cations with EDX so between magnetite (Fe^{2+} and Fe^{3+}) and the Fe-rich wuestite (only Fe^{2+}) cannot be differentiated, especially since magnetite can also incorporate a certain amount of Mg and Mn. These phases are represented by the combined PARC phase wuestite/magnetite. With SEM-EDX light elements (e.g. C, H, O) are difficult to quantify, with the result that portlandite, calcite and free lime cannot be distinguished (PARC phase portlandite/calcite/free lime). Additionally, phases can be intergrown and smaller than the resolution of the EDX (~1 μm) so it is not possible to differentiate them. This is the case for the Si-containing reaction products which, for the autoclaved BOF slag are thought to consist of an intimate intergrowth of hydrogarnets, α-C_2SH, Jaffeite and amorphous C—S—H, as also detected with QXRD.

The highest volume of reaction products is observed in CEM 100 A (63.6 area%) and decreases with increasing amount of BOF slag in the sample to 51 area% in BOFS 100 A. A similar trend is observed in the amount of portlandite/calcite/free lime. The trend of increasing amount of reaction product and portlandite is also observed in the QXRD results (Table 3) and the DOH determination.

Additionally to the phase amounts, it was possible to determine the chemical composition of the different PARC phases in each sample (Table 5) using their PARC sum spectrum [30]. The composition of the remaining, unreacted primary phases in the samples (wuestite/magnetite, C_2S/C_3S and $C_2(A,F)$) agrees well with earlier reported PARC phase compositions of initial and hydrated BOF slag [26,47]. The only exception is the significantly higher TiO_2 content in $C_2(A,F)$ (9.2 wt%)

compared to earlier reported TiO_2 values (5.1 wt%) in C_2(A,F). At the same time, the Al_2O_3 content is somewhat lower (8.6 wt%) compared to the other studies (11.2 wt%). This difference could be the result of not covering a large enough area with PARC, since the bulk composition as measured with XRF shows very similar TiO_2 values (1.38 wt%) compared to the BOF slag used in the earlier studies (1.45 wt%). It is also possible that TiO_2- rich C_2(A,F) is less reactive under autoclaving conditions and predominantly persists as residual primary phase while the Al_2O_3 richer C_2(A,F) has reacted. The other PARC phase compositions are in good agreement with previous reported values [26]. The initial BOF slag phases react in a certain proportion to each other with the water to form the reaction product and no elements are preferentially dissolved from the primary phases and precipitated in the reaction product phase. Hence, no endmembers of a specific phase like the Mg-rich endmember of the wuestite solid solution reacted more than the other, which does not agree with earlier reported findings for the wuestite solid solution series [21].

If the composition of the PARC reaction product is compared between the samples BOFS 100 A has the lowest CaO (48.3 wt%) and Si_2O (22.7 wt%) content, while CEM 100 A has the highest (CaO 57.6 wt%; SiO_2 29.1 wt%). The molar Ca/Si ratios are 2.31 in BOFS 100 A and 2.15 in CEM 100 A. The most significant difference is the high Fe_2O_3* content in the PARC reaction product of BOFS 100 A (15.4 wt%), showing that Fe has been significantly mobilized and was incorporated in the reaction products.

By a thorough analysis of the composition of the reaction product one can conclude that each of the primary BOF slag phases has contributed to form the reaction product in BOFS 100 A, which confirms the DOH calculations. For example the reaction product contains 2.4 and 2.0 wt% MgO and MnO, respectively, which is only present in significant amounts (>2 wt%) in the wuestite/magnetite phase (23.6 wt%). The Al_2O_3 content in the hydration product 1.8 wt%, which is largely contributed by the reaction of C_2(A,F), which is the only Al containing mineral in the initial slag. The hydration product also contains value 3 wt% P_2O_5 whose source is the C_2S.

The relative character of the BOF slag versus CEM I contribution in the reaction product of the BOF 50 A mixture is presented in Table 5 and in the variation diagram of Fig. 8. From the diagram it is clear that the CaO content in the reaction product of BOF 50 A is closer to that of the CEM 100 A, than of BOFS 100 A. The V_2O_5 oxide contribution in BOFS 50 A linearly correlates with the CaO content (straight line for V_2O_5) indicating that the character of the reaction product in BOFS 50 A is closer to that of CEM 100 A than BOFS 100 as it is valid for CaO. To be more specific, that does not mean that the V_2O_5 in the reaction product of BOFS 50 A stems from CEM 1 but that less V_2O_5 is incorporated in the reaction product compared to what would be expected in a 50:50 BOF slag – CEM I mixture. This supports previous findings that V containing C_2S is less reactive than V free C_2S [10]. On the contrary, the signature of Mg- and Si-oxides in the reaction product of BOFS 50 A is strongly determined by BOF slag. It should be noted that MgO in BOFS 50 A (2.6 wt%) is slightly higher than in BOFS 100 A (2.4 wt%). This would lead to the conclusion that the addition of CEM I has a positive effect on the incorporation of MgO into the reaction product of BOFS 50 A. Other oxides like P_2O_5, MnO, SO_3 and Fe_2O_3 have an equal character by BOFS and CEM I (50–60 %), whereas, Al_2O_3 is even stronger dominated than CaO and V_2O_5 by CEM I (for almost 90 %).

3.4. Comparison between the results of QXRD and PARC phase mapping

In order to compare PARC and QXRD results, PARC phases are recalculated from area% to wt%. It is known that area% correspond to volume % [48] and by applying the appropriate phase density to the volume to mass fraction can be made for each PARC phase. For a more detailed description of this method the reader is referred to [47]. For the densities of the phase combinations of wuestite/magnetite, C_3S/C_2S and portlandite/calcite/free lime a weighed mean density was used from the results of QXRD (Table 6). For the PARC reaction product a density was assumed that gives the best agreement with the QXRD results because the density of the amorphous content cannot be determined by QXRD and its determination can be challenging due to their micro and nano porosity [49]. For BOFS 100 A the used density for the PARC reaction product is higher (2.4 g/cm^3) compared to the CEM 100 A (2.1 g/cm^3), which also reflects the higher Fe content in BOFS containing samples, which is incorporated in the reaction products and increases the overall density. Generally the wt% of PARC and the summarized wt% of QXRD are in good agreement with maximum general deviation of about 20 % relatively (Table 6).The deviation between the two results may be related to a too small analyzed area with PARC (~7 mm^2), which may be not as representative for the bulk of the autoclaved material as an XRD sample.

3.5. Pore structure investigation of autoclaved samples

After showing that autoclaving is an effective way to produce large amounts of reaction product in BOF slag containing pastes, it is important to understand why the strength was nevertheless low after autoclaving (BOFS 100 A = 1.4 MPa). Therefore MIP measurements were conducted to investigate the pore structure further.

According to the MIP analysis, the highest cumulative pore volume is observed in the BOFS 100 A sample (~40 vol%). It decreases with the increasing amount of CEM 1 (BOFS 50 A ~ 36 vol% and CEM 100 A 15 vol%). Even though the BOFS 50 A sample contained 50 wt% of CEM 1 in the initial mixing design, the pore structure is more comparable to BOFS 100 A than to CEM 100 A in terms of high cumulative pore volume and pore size distribution (Fig. 9). Both BOF slag samples BOFS 100 A and BOFS 50 A contain mostly large pores, with > 75 vol% of the total pores with a size between 30 and 300 nm. In comparison, the MIP analysis for the CEM 100 A shows that 85 vol% of the pores are below 10 nm.

To summarize, the pore structure is the clear cause for the low mechanical strength of the autoclaved BOF slag containing samples The negative correlation between porosity and mechanical strength in cementitious systems has been widely documented [50–52]. Researchers have previously reported that the formation of α-C_2SH is undesirable in sand lime bricks due its low strength and its platy habitus causing significant pore space [35]. However, α-C_2SH is not the main reason for the high porosity and the resulting poor mechanical performance. The BOFS 50 A sample contains significantly more α-C_2SH (23 wt%) and has a lower cumulative pore volume (36 vol%) compared to BOFS 100 A with 15 wt% and 40 vol%,respectively. In contrast BOFS 50 A (12.7 MPa) has higher compressive strength than BOFS 100 A (1.4 MPa). More likely is that the amount of unconsumed water that has evaporated and left behind the pore space is causing the poor mechanical performance [53,54] of BOF slag containing samples. This is visible in the results of the TGA analysis, whereas CEM 100 G and A have significantly higher weight loss up to 1000 °C (>17 wt%) compared to the BOF slag containing samples (<10 wt%). The significant difference in volatile loss during TGA (>70 %) and hence the significant difference in unbound water in BOFS slag may be the main reason for the difference in porosity between CEM 100 A and autoclaved BOF slag containing samples.

3.6. Leaching analysis of the autoclaved material

The XRF analysis of the used raw materials showed that the BOF slag contains significant amounts of Cr and V (Table 1). Even though, the toxicity of the elements Cr and V heavily depends on their oxidation state [55,56], a one batch leaching test will give an insight in the potential restrictions of autoclaved BOF slag as an environmental sustainable building material. Table 7 reports the results of the one batch leaching test for a selection of the most concerning elements and their respective legal limits in the Netherlands according to the Dutch Soil Quality Decree (DSQD) [57]. In both autoclaved BOF slag samples Cr is below the DSQD limits of 0.63 mg/kg. V concentrations for both leachates of the autoclaved BOF slag containing samples are below the detection limit of the ICP-OES (V detection limit = 0.01 mg/kg). The results show that the reaction products that form during autoclaving may incorporate Cr and V and effectively immobilizes these elements. Previously it has been shown that hydrothermal C—S—H phases may incorporate heavy metal elements [58]. That Cr and V are effectively incorporated in the reaction products that formed during autoclaving is also proven by the composition of the PARC reaction product (Table 5).

4. Conclusions

In this study, the reactivity of BOF slag as a binder under autoclave conditions was investigated. With our multi analytical approach we have investigated and were able to compare the reactivity and reaction products after 72 h of curing at room temperature (72 h) and after autoclaving at 11 bar and 187 °C for 8 h. The following conclusions can be made:

- Autoclaving of BOF slag containing samples causes an increase in compressive strength (e.g. BOFS 100 G, 0.1 MPa; BOFS 100 A, 1.4 MPa). However, the final achieved strength in autoclaved BOF slag containing paste samples is still low (<15 MPa).
- Autoclaving is very effective in increasing the degree of hydration. The degree of hydration for BOF slag containing samples almost triples (BOFS 100 G, 11.8 wt%; BOFS 100 A, 33.2 wt%), whereas the amount of bound water in the BOFS 100 samples more than doubles (BOFS 100 G, 2.8 wt%; BOFS 100 A, 6.2 wt%). This illustrates the increased hydraulic reactivity of BOF slag under autoclave conditions.
- The main reaction products that developed in the autoclaved BOF slag containing samples were hydrogarnet (BOFS 100 A, 7.3 wt%), α-C_2SH (BOFS 100 A, 15 wt%) and amorphous (BOFS 100 A, 17 wt %).
- The PARC analysis gives a bulk chemical composition for the Si-containing reaction products, which shows that the initial BOF slag phases (C_2S, $C_2(A,F)$ and wuestite) are all reactive under autoclave conditions and contribute to the Si-containing reaction products.
- Even though large amounts of reaction products (>40 wt%) formed in the autoclaved BOFS slag containing samples large amounts of spore space developed based on MIP results (BOFS 100 A, 40 vol%) explaining the poor mechanical performance. Even though α-C_2SH is known to be a phase associated with porosity. The main control on the large amount of porosity is the amount of unconsumed water during the reactions in the autoclave.

As future recommendations, we propose three possible options. The first option is to further investigate the performance of BOFS slag based autoclaved building material products with the addition of a Si source and variable autoclave conditions. As many authors proposed before that Ca/Si ratio and the autoclave conditions are the most controlling factors on the mechanical properties [25,35,38]. The second option to produce a product based on BOF slag would be by increasing the reactivity to the BOF slag binder by chemical [26] or mechanochemical [59] activation in order to reduce the free water and increase the amount of reaction product during the autoclave process. This would probably reduce the porosity and increase mechanical performance. The third option would be the use of the of the BOF slag based product as a binder itself as α-C_2SH is a major component in new hydrothermally activated binder systems [60,61].

CRediT authorship contribution statement

J.C.O. Zepper: Conceptualization, Data curation, Methodology, Writing – original draft. **S.R. van der Laan:** Supervision, Funding acquisition, Project administration, Writing – review & editing. **K. Schollbach:** Conceptualization, Supervision, Data curation, Writing – review & editing. **H.J.H. Brouwers:** Supervision, Funding acquisition, Project administration.

Declaration of Competing Interest

The authors declare the following financial interests/personal relationships which may be considered as potential competing interests: Jonathan Zepper reports financial support was provided by M2i Materials Innovation Institute. Jonathan Zepper reports a relationship with Eindhoven University of Technology that includes: employment.

Data availability

Data will be made available on request.

Acknowledgement

The authors would like to express their gratitude for the financial support of the Nederlandse Organisatie voor Wetenschappelijk Onderzoek (NWO) by funding this research (project no.10023338) and Materials Innovation Institute (M2i) for managing this project. Furthermore, the authors would like to acknowledge the following sponsors of this research: Tata Steel; ENCI; V.d. Bosch Beton; Beton Mortel; Inashco; Hess AAC systems. The recognition for helping with the autoclave treatment of the samples belongs to Ladislaus Heinz of Hess AAC Systems. A special thanks goes to Frank van der Does of Tata Steel Ijmuiden for the SEM/EDS sample preparation and measurement. Moreover, Anneke Delsing at TU Eindhoven is thanked for the analysis of the leachates with ICP-OES.

Appendix A

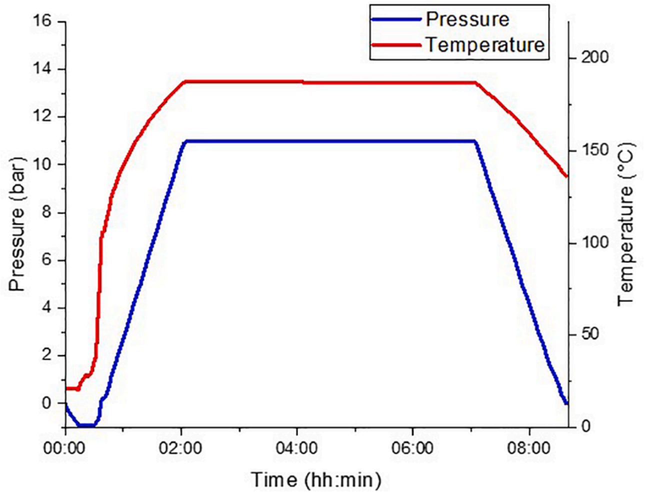

Fig. A1. Presents the pressure and temperature conditions of the autoclave treatment.

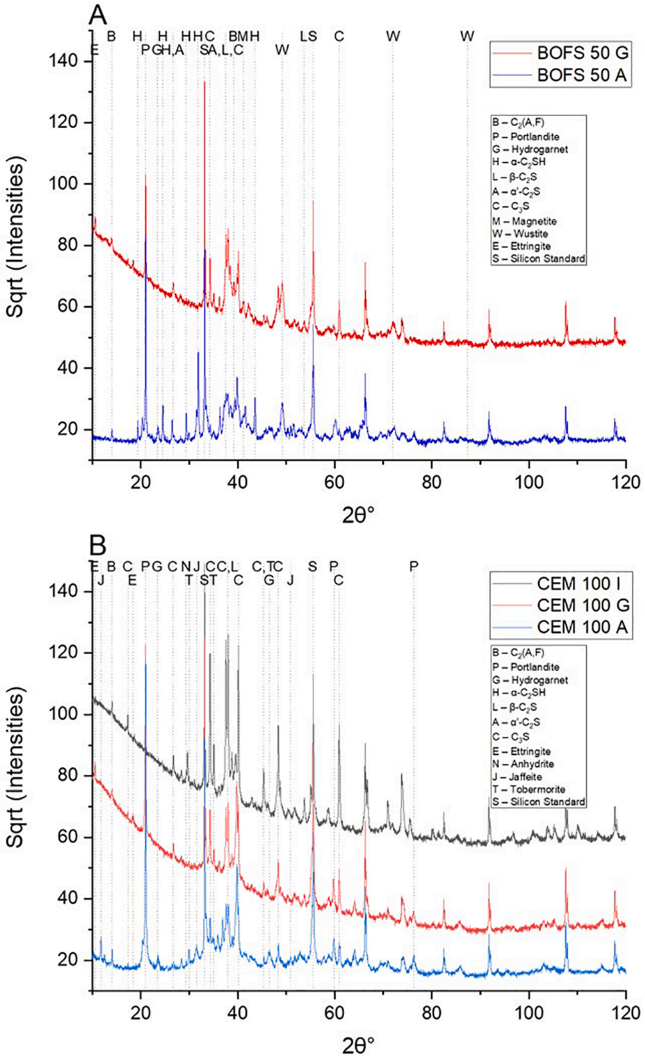

Fig. A2. A (top) illustrates XRD patterns of BOFS 50 G (red,) and BOFS 50 A (blue), B (bottom) illustrates XRD patterns of CEM 100 I (black), CEM 100 G (red) and BOFS 100 A (blue) and the respective identified phases (legends on the right).

Table A1
Gives mineral name, cement notation and AMCS/CSD/PDF data code of used crystal structures for the QXRD. For C_2S and hydrogarnet two structures were used.

Mineral Name	Cement Notation	AMCS	ICSD	PDF-Nr.
Si-Standard		0011243		
Wuestite	RO-Phase	0011314		
C_2S	C_2S	0012179 (β-C2S)	81097 (α'-C2S)	
Magnetite	Ff		30860	
$C_2(A,F)$	$C_2(A,F)$			04-014-6627
C_3S	C_3S	0017753		
Free Lime	C	0008276		
Portlandite	CH	0000117		
Calcite	Cc	0000098		
C_3A	C_3A	0009531 (cubic)		
Hydrogarnet	$C_3(A,F)S_{3-x}H_{2x}$	0001827 (Katoite)		75-1410 (Hydroandradite)
Ettringite	$C_6AS_3H_{32}$	0009368		
Jaffeite	$C_6S_2H_3$	0012342		
Tobermorite (9A)	$C_5S_6H_5$		87689	
α-C_2SH	C_2SH	0010292		
Brucite	Mc	0014731		
Metavauxite	fAP_2H_9	0012432		
Others				
Ferrite	–		76747	
Fe-Perovskite	C_3TF			04-019-5637
Dolomite	CMc_2	0000086		

References

[1] H. Jalkanen, L. Holappa, Converter Steelmaking, in: S. Seetharaman, A. McLean, R. Guthrie, S. Sridhar (Eds.), Treatise Process Metall. Ind. Process. vol. 3, Elsevier Ltd., Oxford, 2014, pp. 223–270, https://doi.org/10.1016/B978-0-08-096988-6.00014-6.

[2] L.M. Juckes, Transactions of the Institutions of Mining and Metallurgy: Section C. The volume stability of modern steelmaking slags, Miner. Process. Extr. Metall. 112 (2003) 177–197, https://doi.org/10.1179/037195503225003709.

[3] G. Wang, Y. Wang, Z. Gao, Use of steel slag as a granular material : Volume expansion prediction and usability criteria, J. Hazard. Mater. 184 (2010) 555–560, https://doi.org/10.1016/j.jhazmat.2010.08.071.

[4] T.-H. Lu, Y. Chen, P. Shih, J. Chang, Use of basic oxygen furnace slag fines in the production of cementitious mortars and the effects on mortar expansion, Constr. Build. Mater. 167 (2018) 768–774, https://doi.org/10.1016/j.conbuildmat.2018.02.102.

[5] J. Zhao, P. Yan, D. Wang, Research on mineral characteristics of converter steel slag and its comprehensive utilization of internal and external recycle, J. Clean. Prod. 156 (2017) 50–61, https://doi.org/10.1016/j.jclepro.2017.04.029.

[6] S. Wang, C. Wang, Q. Wang, Z. Liu, W. Qian, C.Z. Jin, et al., Study on cementitious properties and hydration characteristics of steel slag, Polish J. Environ. Stud. 27 (2018) 357–364, https://doi.org/10.15244/pjoes/74133.

[7] J.N. Murphy, T.R. Meadowcroft, M.R. de Assis, P.V. Barr, Enhancement of the cementitious properties of steelmaking slag, Can. Metall. Q. 36 (1997) 315–331, https://doi.org/10.1179/cmq.1997.36.5.315.

[8] E. Belhadj, C. Diliberto, A. Lecomte, Characterization and activation of Basic Oxygen Furnace slag, Cem. Concr. Compos. 34 (2012) 34–40, https://doi.org/10.1016/j.cemconcomp.2011.08.012.

[9] K. Schraut, B. Adamczyk, C. Adam, D. Stephan, B. Meng, S. Simon, et al., Cement and Concrete Research Synthesis and characterisation of alites from reduced basic oxygen furnace slags, Cem. Concr. Res. 147 (2021), https://doi.org/10.1016/j.cemconres.2021.106518. Received.

[10] M.J. Ahmed, R. Cuijpers, K. Schollbach, S. Van der Laan, M. Van Wijngaarden-Kroft, T. Verhoeven, et al., V and Cr Substitution in Dicalcium Silicate (C2s) Under Oxidizing and Reducing Conditions- Synthesis, Reactivity, and Leaching Behaviour Studies, J. Hazard. Mater. 442 (2022), 130032, https://doi.org/10.2139/ssrn.4134122.

[11] S. Zhuang, Q. Wang, Inhibition mechanisms of steel slag on the early-age hydration of cement, Cem. Concr. Res. 140 (2021), https://doi.org/10.1016/j.cemconres.2020.106283.

[12] Y. Jiang, T.C. Ling, C. Shi, S.Y. Pan, Characteristics of steel slags and their use in cement and concrete—A review, Resour. Conserv. Recycl. 136 (2018) 187–197, https://doi.org/10.1016/j.resconrec.2018.04.023.

[13] O. Gencel, O. Karadag, O.H. Oren, T. Bilir, Steel slag and its applications in cement and concrete technology: A review, Constr. Build. Mater. 283 (2021), 122783, https://doi.org/10.1016/j.conbuildmat.2021.122783.

[14] H. Grundlach, Dampfgehärtete Bustoffe. First Edit, Bauverlag GmbH, Wiesbaden, Germany, 1972.

[15] H. Yazıcı, E. Deniz, B. Baradan, The effect of autoclave pressure, temperature and duration time on mechanical properties of reactive powder concrete, Constr. Build. Mater. 42 (2013) 53–63, https://doi.org/10.1016/j.conbuildmat.2013.01.003.

[16] Y. Fang, Y. Gu, Q. Kang, Q. Wen, P. Dai, Utilization of copper tailing for autoclaved sand-lime brick, Constr. Build. Mater. 25 (2011) 867–872, https://doi.org/10.1016/j.conbuildmat.2010.06.100.

[17] T. Cicek, M. Tanriverdi, Lime based steam autoclaved fly ash bricks, Constr. Build. Mater. 21 (2007) 1295–1300, https://doi.org/10.1016/j.conbuildmat.2006.01.005.

[18] H. Motz, J. Geiseler, Products of steel slags an opportunity to save natural resources, Waste Manag. 21 (2001) 285–293.

[19] Q. Zhao, J. Stark, E. Freyburg, M. Zhou, Steam and Autoclave Treatments on Structure Characteristics of Steel Slag 356–360 (2012) 1919–1927, https://doi.org/10.4028/www.scientific.net/AMR.356-360.1919.

[20] Q. Wang, M. Shi, Z. Zhang, Hydration properties of steel slag under autoclaved condition, J. Therm. Anal. Calorim. 120 (2015) 1241–1248, https://doi.org/10.1007/s10973-015-4397-3.

[21] G.R. Qian, D.D. Sun, J.H. Tay, Z.Y. Lai, Hydrothermal reaction and autoclave stability of Mg bearing RO phase in steel slag, Br. Ceram. Trans. 101 (2002) 159–164, https://doi.org/10.1179/096797802225003415.

[22] Y.L. Chen, C.T. Lin, Recycling of basic oxygen furnace slag as a raw material for autoclaved aerated concrete production, Sustain 12 (2020), https://doi.org/10.3390/SU12155896.

[23] E.R. Buckle, H.F.W. Taylor, The Hydration of tricalcium and b-dicalcium silicates in pastes under normal and stean curing conditions, J. Appl. Chem. 9 (1959) 163–172, https://doi.org/10.1002/jctb.5010090306.

[24] B.Z. Dilnesa, B. Lothenbach, G. Renaudin, A. Wichser, D. Kulik, Synthesis and characterization of hydrogarnet Ca3(Al xFe1 - X)2(SiO4)y(OH) 4(3 - y), Cem. Concr. Res. 59 (2014) 96–111, https://doi.org/10.1016/j.cemconres.2014.02.001.

[25] N. Meller, K. Kyritsis, C. Hall, The mineralogy of the CaO-Al2O3-SiO2-H2O (CASH) hydroceramic system from 200 to 350 °C, Cem. Concr. Res. 39 (2009) 45–53, https://doi.org/10.1016/j.cemconres.2008.10.002.

[26] A.M. Kaja, K. Schollbach, S. Melzer, S.R. van der Laan, H.J.H. Brouwers, Q. Yu, Hydration of potassium citrate-activated BOF slag, Cem. Concr. Res. 140 (2021) 1–11, https://doi.org/10.1016/j.cemconres.2020.106291.

[27] P.Y. Mahieux, J.E. Aubert, G. Escadeillas, M. Measson, Quantification of Hydraulic Phase Contained in a Basic Oxygen Furnace Slag, J. Mater. Civ. Eng. 26 (2014) 593–598, https://doi.org/10.1061/(asce)mt.1943-5533.0000867.

[28] E. Belhadj, C. Diliberto, A. Lecomte, Properties of hydraulic paste of basic oxygen furnace slag, Cem. Concr. Compos. 45 (2014) 15–21, https://doi.org/10.1016/j.cemconcomp.2013.09.016.

[29] K. Scrivener, R. Snellings, B. Lothenbach. A Practical Guide to Microstructural Analysis of Cementitious Materials, CRC Press, Boca Raton, FL, United States, 2016, https://doi.org/10.1201/b19074.

[30] C. van Hoek, J. Small, S. van der Laan, Large-Area Phase Mapping Using P h A se R ecognition and C haracterization (PARC) Software, Micros Today 24 (2016) 12–21, https://doi.org/10.1017/s1551929516000572.

[31] O.A. Alawad, A. Alhozaimy, M.S. Jaafar, F.N.A. Aziz, A. Al-Negheimish, Effect of Autoclave Curing on the Microstructure of Blended Cement Mixture Incorporating Ground Dune Sand and Ground Granulated Blast Furnace Slag, Int. J. Concr. Struct. Mater. 9 (2015) 381–390, https://doi.org/10.1007/s40069-015-0104-9.

[32] H.F.W. Taylor, The calcium silicate hydrates, in: H.F.W. Taylor (Ed.), Chem. Cem, 1st ed.,, Academic Press, London, UK, 1964, pp. 168–232.

[33] S.Y. Hong, F.P. Glasser, Phase relations in the CaO-SiO2-H2O system to 200 °C at saturated steam pressure, Cem. Concr. Res. 34 (2004) 1529–1534, https://doi.org/10.1016/j.cemconres.2003.08.009.

[34] G. Carter, D.K. Smith, Properties of cementing compositions at elevated temperatures and pressure, Pet. Trans. AIME 213 (1958) 20–27, https://doi.org/10.2118/892-g.

[35] H.F.W. Taylor, Cement Chem. 20 (1998) 9465.

[36] D.C.S. Garcia, K. Wang, R.B. Figueiredo, The influences of quartz content and water-to-binder ratio on the microstructure and hardness of autoclaved Portland cement pastes, Cem. Concr. Compos. 91 (2018) 138–147, https://doi.org/10.1016/j.cemconcomp.2018.05.010.

[37] B. Ilić, A. Mitrović, L. Miličić, M. Zdujić, Compressive strength and microstructure of ordinary cured and autoclaved cement-based composites with mechanically activated kaolins, Constr. Build. Mater. 178 (2018) 92–101, https://doi.org/10.1016/j.conbuildmat.2018.05.144.

[38] H. Tian, D. Stephan, B. Lothenbach, C. Lehmann, Influence of foreign ions on calcium silicate hydrate under hydrothermal conditions: A review, Constr. Build. Mater. 301 (2021), 124071, https://doi.org/10.1016/j.conbuildmat.2021.124071.

[39] A. Hartmann, Untersuchungen zum Kristallisationsverhalten und zur Morphologie von 11 Å Tobermorit in Abhängigkeit von der Reaktivität der Kieselsäurequelle und dem Ionenbestand der Hydrothermallösung, University of Hannover, 2004.

[40] R. Gendvilas, R. Siauciunas, K. Baltakys, Quantitative thermal analysis of α-C2SH as a precursor for low-energy cements, J. Therm. Anal. Calorim. 121 (2015) 155–162, https://doi.org/10.1007/s10973-015-4570-8.

[41] D.S. Klimesch, A. Ray, Evaluation of phases in a hydrothermally treated CaO-SiO2-H2O system, J. Therm. Anal. Calorim. 70 (2002) 995–1003, https://doi.org/10.1023/A:1022289111046.

[42] S. Shaw, C.M.B. Henderson, B.U. Komanschek, Dehydration/recrystallization mechanisms, energetics, and kinetics of hydrated calcium silicate minerals: An in situ TGA/DSC and synchrotron radiation SAXS/WAXS study, Chem. Geol. 167 (2000) 141–159, https://doi.org/10.1016/S0009-2541(99)00206-5.

[43] H. Sabeur, M. Saillio, J. Vincent, Thermal stability and microstructural changes in 5 years aged cement paste subjected to high temperature plateaus up to 1000 °C as studied by thermal analysis and X-ray diffraction, Heat Mass Transf. 55 (2019) 2483–2501, https://doi.org/10.1007/s00231-019-02599-w.

[44] H. Sabeur, G. Platret, J. Vincent, The effect of ageing and heat treatment on microstructure evolution of a commercial cement paste, Heat Mass Transf. 53 (2017) 2609–2626, https://doi.org/10.1007/s00231-017-2004-9.

[45] Q. Wang, P. Yan, J. Feng, A discussion on improving hydration activity of steel slag by altering its mineral compositions, J. Hazard. Mater. 186 (2011) 1070–1075, https://doi.org/10.1016/j.jhazmat.2010.11.109.

[46] Q. Wang, P.Y. Yan, S. Han, The influence of steel slag on the hydration of cement during the hydration process of complex binder, Sci. China Technol. Sci. 54 (2011) 388–394, https://doi.org/10.1007/s11431-010-4204-0.

[47] H. Pöllmann, Industrial Waste, de Gruyter, Berlin, Germany, 2021.

[48] M.D. Higgins, Quantitative Textural Measurements in Igneous and Metamorphic Petrology, Cambridge University Press, New York, United States, 2006, https://doi.org/10.1017/CBO9780511535574.

[49] A.J. Allen, J.J. Thomas, H.M. Jennings, Composition and density of nanoscale calcium-silicate-hydrate in cement, Nat. Mater. 6 (2007) 311–316, https://doi.org/10.1038/nmat1871.

[50] K. Kendall, A.J. Howard, J.D. Birchall, Relation Between Porosity, Microstructure and Strength, and the Approach To Advanced Cement-Based Materials, Phil. Trans. R. Soc. Lond. A 310 (1983) 139–153, https://doi.org/10.1098/rsta.1983.0073.

[51] J.J. Beaudoin, R.F. Feldman, P.J. Tumidajski, Pore structure of hardened portland cement pastes and its influence on properties, Adv. Cem. Bas. Mat. 1 (1994) 224–236, https://doi.org/10.1016/1065-7355(94)90028-0.

[52] P.C. Hewlett, M. Liska, P.-C. Aïtcin, J.J. Beaudoin, J. Bensted, J.S.J. van Deventer, et al.. Lea“ s Chemistry of Cement and Concrete 5th ed., vol. 58, Butterworth-Heinemann, Oxford, 2019.

[53] H. Ma, B. Xu, Z. Li, Magnesium potassium phosphate cement paste: Degree of reaction, porosity and pore structure, Cem. Concr. Res. 65 (2014) 96–104, https://doi.org/10.1016/j.cemconres.2014.07.012.

[54] M. Lizcano, A. Gonzalez, S. Basu, K. Lozano, M. Radovic, Effects of water content and chemical composition on structural properties of alkaline activated metakaolin-based geopolymers, J. Am. Ceram. Soc. 95 (2012) 2169–2177, https://doi.org/10.1111/j.1551-2916.2012.05184.x.

[55] S.E. Fendorf, Surface reactions of chromium in soils and waters, Geoderma 67 (1995) 55–71, https://doi.org/10.1016/0016-7061(94)00062-F.

[56] D.H. McNear, R. Tappero, D.L. Sparks, Shining light on metals in the environment, Elements 1 (2005) 211–216, https://doi.org/10.2113/gselements.1.4.211.

[57] Overheid.nl. Regeling bodemkwaliteit. 2015.

[58] T. Dambrauskas, I. Knabikaite, A. Eisinas, K. Baltakys, M.T. Palou, Influence of Cr3 +, Co2+ and Cu2+ on the formation of calcium silicates hydrates under hydrothermal conditions at 200 °C, J. Asian Ceram. Soc. 8 (2020) 753–763, https://doi.org/10.1080/21870764.2020.1789287.

[59] X. Zhu, H. Hou, X. Huang, M. Zhou, W. Wang, Enhance hydration properties of steel slag using grinding aids by mechanochemical effect, Constr. Build. Mater. 29 (2012) 476–481, https://doi.org/10.1016/j.conbuildmat.2011.10.064.

[60] R. Siauciunas, J. Mikaliunaite, L. Urbonas, K. Baltakys, Tribochemical and thermal activation of α-c2s hydrate as precursor for cementitious binders, J. Therm. Anal. Calorim. 118 (2014) 817–823, https://doi.org/10.1007/s10973-014-3921-1.

[61] K. Garbev, G. Beuchle, U. Schweike, D. Merz, O. Dregert, P. Stemmermann, Preparation of a novel cementitious material from hydrothermally synthesized C-S-H phases, J. Am. Ceram. Soc. 97 (2014) 2298–2307, https://doi.org/10.1111/jace.12920.